

The coastal winds off western subtropical South America in future climate scenarios

René D. Garreaud* and Mark Falvey

Department of Geophysics, Universidad de Chile, Santiago, Chile

ABSTRACT: The west coast of subtropical South America is characterized by a semi-arid climate and very persistent southerly winds that often exhibit a low-level jet structure. The nearly alongshore flow forces coastal and offshore upwelling of cold, nutrient-rich waters, thus supporting one of the most productive marine ecosystems in the world and a wealth of fishery resources. Therefore, the evaluation of the changes in the coastal winds in future climate is a key step to predict the regional environmental impacts of global climate change linked to anthropogenic greenhouse gas (GHG) increases.

In this work we document the wind changes between present-day conditions and those projected for the end of the 21st century under two Intergovernmental Panel on Climate Change (IPCC) scenarios (A2 and B2). We first estimate and interpret the changes of the wind field over the southeast Pacific from 15 coupled atmosphere–ocean Global Circulation Models (GCMs). Very consistent among the GCMs is the strengthening of the southerlies along the subtropical coast as a result of a marked increase in surface pressure farther south. We then examine the coastal wind changes in more detail using the Providing Regional Climate for Impact Studies (PRECIS) regional climate model (RCM) with 25 km horizontal resolution nested in the Hadley Centre Atmospheric global Model (HadAM3). PRECIS results indicate that the largest southerly wind increase occurs between 37–41°S during spring and summer, expanding the upwelling-favourable regime in that region, at the same time that coastal jets at subtropical latitudes will become more frequent and last longer than current events. During fall and winter, the strengthening of the southerlies occurs at subtropical latitudes maintaining a mean jet year-round. Finally, we discuss the possibility that strengthening of the coastal southerlies might actually lead to a relative regional cooling even as the world as a whole continues to warm up. Copyright © 2008 Royal Meteorological Society

KEY WORDS coastal winds; upwelling; South America; Chile; climate change; PRECIS

Received 9 August 2007; Revised 3 April 2008; Accepted 7 April 2008

1. Introduction

There are an increasing number of studies addressing the local- and regional-scale impacts of the GHG-related global climate change (see reviews Christensen *et al.*, 2007). Most of these studies focus on the potential changes in temperature and precipitation because of their direct and profound societal and environmental impacts. For the subtropical coast of western South America (25–35°S, north-central Chile), however, the most important impacts may be associated with changes in the surface wind regime. On one hand, the region has a very arid climate and model-based predictions for the 21st century do not show any significant change in such conditions (e.g. Fuenzalida *et al.*, 2007). On the other hand, the predominantly southerly winds are a key ingredient of the regional environment as they force upwelling of cold, nutrient-rich waters along this nearly north-south oriented coastline, thus supporting one of the most productive marine ecosystems in the world and a wealth of fishery resources (e.g. Rutllant and Montecino,

2002; Yuras *et al.*, 2005). The wind field itself often exhibits a mesoscale coastal jet structure off central Chile (Garreaud and Muñoz, 2005), producing a particularly favourable environment for enhanced sea surface cooling and oceanic eddy generation (e.g. Chaigneau and Pizarro, 2005). The variability of the coastal winds is in turn associated with changes in the position and intensity of the subtropical southeast (SE) Pacific anticyclone and sea level pressure (SLP) anomalies farther south (Muñoz and Garreaud, 2005).

In this work, we study the changes in the surface wind field off western subtropical South America in future climate scenarios, and explore their possible impacts on sea surface temperature (SST). An overview of the present-day atmospheric coastal circulation is provided in Section 2. We then address the changes between present-day conditions and those projected for the end of the 21st century (2071–2100) for two Intergovernmental Panel on Climate Change (IPCC) scenarios: Special Report on Emissions Scenarios (SRES) A2 and B2 (Nakicenovic and Swart, 2000). In Section 3, a first estimate of the changes in the coastal wind is derived from coupled atmosphere–ocean GCMs outputs. Results from more than a dozen coupled GCMs are currently available

* Correspondence to: René D. Garreaud, Department of Geophysics, Universidad de Chile, Blanco Encalada 2002, Santiago, Chile.
E-mail: rgarreau@dgf.uchile.cl

allowing us to examine the consistency of specific climatic projection among the models. Nevertheless, most GCMs have a horizontal grid spacing coarser than 200 km, and therefore, they tend to miss mesoscale details of the wind field that are important for the coastal upwelling. A more detailed picture of the changes is obtained in Section 4 from the results of a regional climate model (RCM) that was also run for 2071–2100 time slice for the A2 and B2 scenarios. Here we have used the Providing REgional Climate for Impact Studies (PRECIS); (Jones *et al.*, 2004) RCM with a 25-km grid spacing and forced by the Hadley Centre Atmospheric Model version 3 (HadAM3); (Pope *et al.*, 2001) at their lateral boundaries. PRECIS is, however, an atmospheric-only model, so the possible changes in SST are discussed in Section 5 using a ‘conceptual-downscaling’ of our PRECIS results, as well as an examination of the outputs from coupled GCMs. A summary of our main findings is presented in Section 6.

2. Coastal circulation overview

In this section, we provide an observational overview of the low-level circulation off the subtropical west coast of South America; a more detailed description of the

circulation is presented in Garreaud and Muñoz, 2005, (GM05). Our primary database is the version-3 QuikScat surface wind stress fields for the period January 2000 to December 2005, obtained from Remote Sensing Systems (www.ssmi.com). Specifically, we used daily fields of sea surface wind components (u_s and V_s) and wind speed (w_s) on a $0.25^\circ \times 0.25^\circ$ latitude–longitude regular grid. Monthly averages are denoted by capital letters (e.g. W_s). Monthly mean SLP and wind were obtained from the NCEP/NCAR reanalysis (Kalnay *et al.*, 1996) for the period 1960–2005. In spite of its coarse horizontal resolution ($2.5^\circ \times 2.5^\circ$), reanalysis data do capture the mean seasonal cycle and the inter-annual variability of the meridional wind off central Chile.

The subtropical (25° – 35° S) coast is under the influence of the SE Pacific anticyclone resulting in very persistent low-level southerly winds year-round (Figures 1(a) and 2(a)). As the coastline is approximately north–south oriented, and the centre of the anticyclone is about 1000 km to the west of the continent, the surface wind field forces upwelling of cold waters along the coast (due to Ekman transport) and farther offshore (due to Ekman pumping) (e.g. Shaffer *et al.*, 1999). The cold waters along the coast also contribute to the formation of an intense air temperature inversion with its base at ~ 600 m,

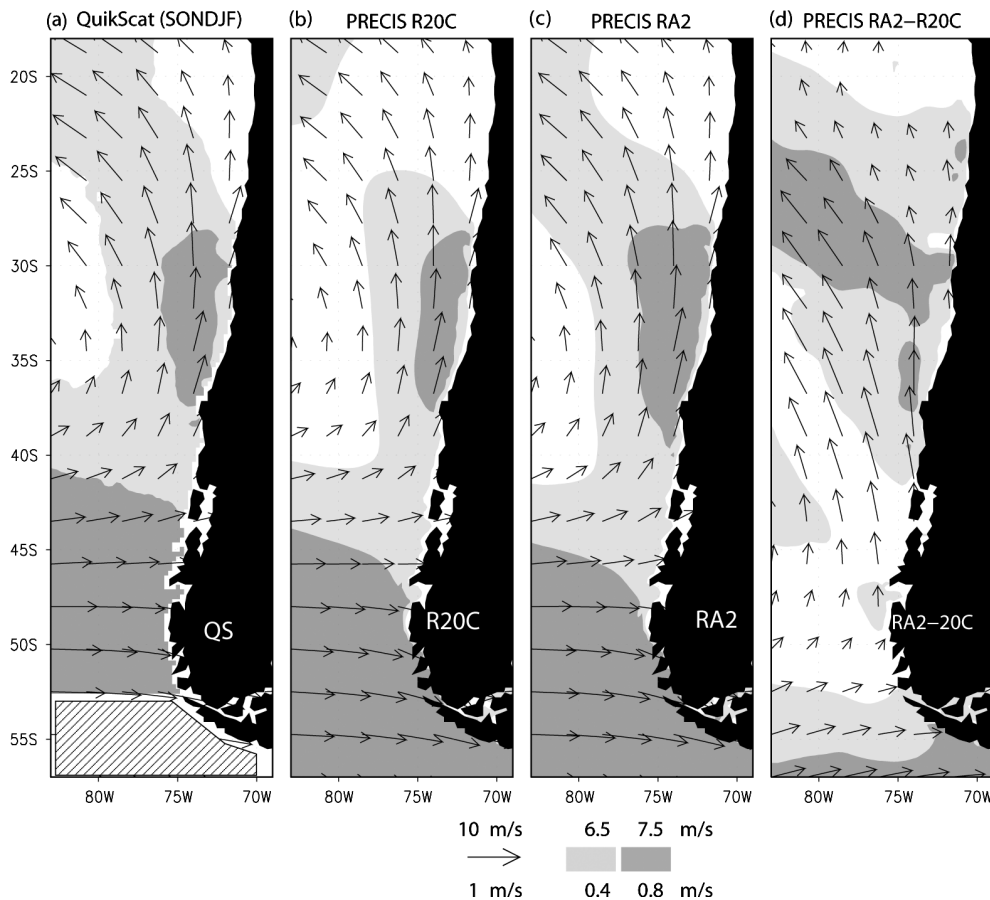


Figure 1. Long-term mean surface winds (arrows, scale at the bottom, upper row) and surface wind speed (shaded, scale at the bottom, upper row) for spring/summer (September to February) using (a) QuikScat data (2000–2005), (b) PRECIS R20C simulation (1961–1990), and (c) PRECIS RA2 simulation (2071–2100). Hatched area in panel (a) indicates no QuikScat data. Panel (d) shows the surface wind (arrows, scale at the bottom, lower row) and surface wind speed (shaded, scale at the bottom, lower row) difference between PRECIS simulations RA2 minus R20C.

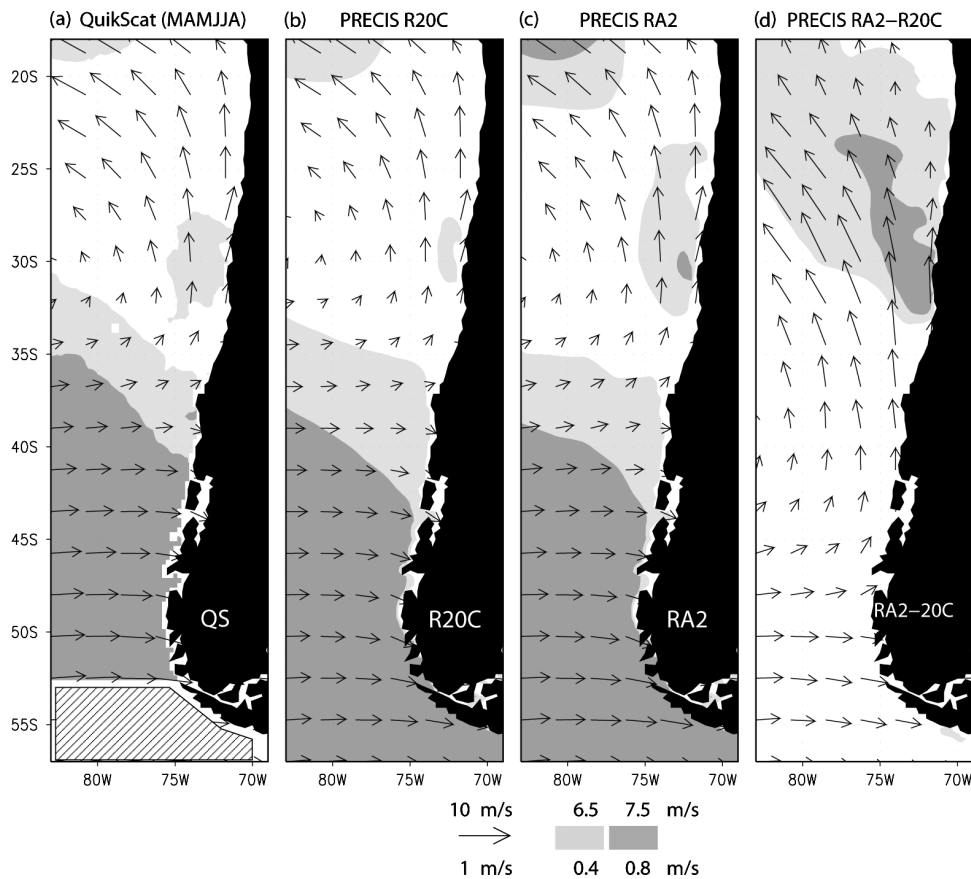


Figure 2. Long-term mean surface winds (arrows, scale at the bottom, upper row) and surface wind speed (shaded, scale at the bottom, upper row) for fall/winter (March to August) using (a) QuikScat data (2000–2005), (b) PRECIS R20C simulation (1961–1990), and (c) PRECIS RA2 simulation (2071–2100). Hatched area in panel (a) indicates no QuikScat data. Panel (d) shows the surface wind (arrows, scale at the bottom, lower row) and surface wind speed (shaded, scale at the bottom, lower row) difference between PRECIS simulations RA2 minus R20C.

capping the cool marine boundary layer (MBL); (Garreaud and Muñoz, 2005). The prevalence of southerly winds decreases pole-ward along the coast due to the passage of mid-latitude weather systems. At 40°S (the southern limit of our study region) the monthly mean southerlies are restricted to austral summer.

Daily wind fields often exhibit a meridionally elongated southerly jet off the subtropical coast, where surface wind speed can reach up to $\sim 15 \text{ m s}^{-1}$ (twice the climatological mean). The jet core is located at the top of the MBL, has a cross-shore scale of about 300 km and its axis is about 100 km off the coast (GM05). Coastal jets are observed about 60% of the time during austral spring and summer, clustered in events that last between 3 and 7 days, and they generally cause a marked cooling of the sea surface (Renault *et al.*, 2007). Because jet events occur frequently and with recurrent positioning from September to February, the long-term monthly means also exhibit a coastal jet structure (Figure 1(a)). During fall and winter, jets are observed less often (30% of the time) and interrupted by periods of very weak southerly or even northerly winds. Consistently, the long-term monthly means from March to August only hint at a coastal jet structure (Figure 2(a)).

The occurrence of a southerly jet is linked to the passage of a surface anticyclone at mid-latitudes producing a

north-south pressure gradient along the coast (Muñoz and Garreaud, 2005). The very steep coastal terrain precludes the development of low-level easterly (cross-shore) flow that would geostrophically balance this pressure gradient. Instead, the meridional (southerly) flow accelerates until turbulent friction in the MBL balances the pressure gradient force. Changes in the meridional pressure gradient explain more than 80% of the day-to-day variability of the surface wind speed off the coast (Muñoz and Garreaud, 2005). The ageostrophic relationship also holds at intra-seasonal and inter-annual timescales, as suggested by the scatter plot (Figure 3) between monthly mean values of W_s at 33°S–74°W and the SLP difference between 38° and 28°S along 74°W (SLP_y). Considering monthly mean values from November to February, there is a significant correlation ($r = 0.67$) between these variables, with a fitted-line slope of $\partial W_s / \partial SLP_y \sim 1 \text{ m s}^{-1} / \text{hPa}$.

3. Coastal winds in coupled GCMs

A first estimate of the potential changes in the coastal wind circulation is obtained from the outputs of 15 coupled GCMs (see Table I for details), a representative subset of the integrations in the World Climate Research Programme's (WCRP's) Coupled Model Intercomparison Project phase 3 (CMIP3) multi-model dataset (see

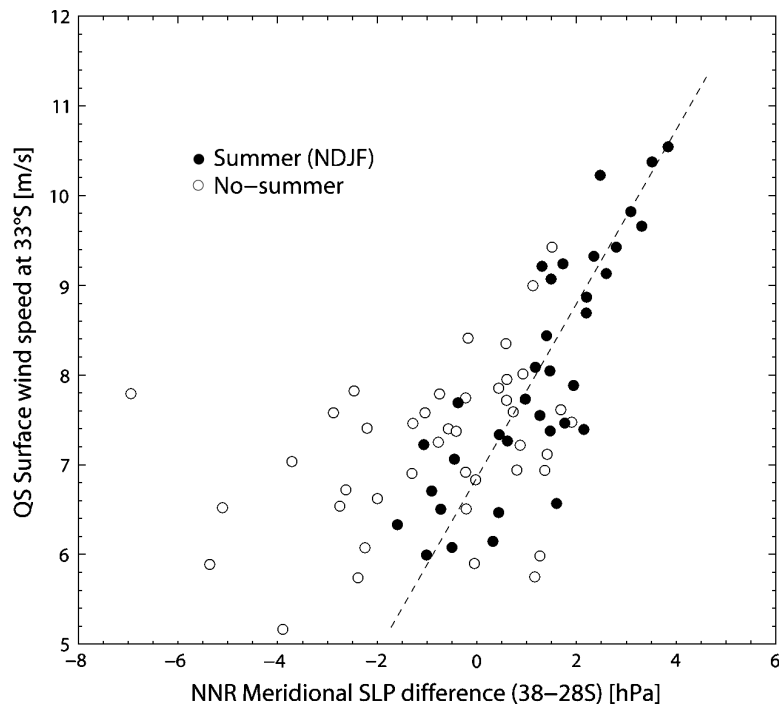


Figure 3. Scatter plot between monthly mean values of NCEP-NCAR reanalysis gross SLP meridional pressure gradient along 74°W (horizontal axis) and QuikScat surface wind speed at 33°S – 74°W (vertical axis). The gross gradient was calculated as the SLP difference between 38°S and 28°S . Data pairs for all months from January 2000 to December 2005 are plotted. Filled circles indicate data pairs for summer months (November to February); open circles indicate data pairs for the rest of the months.

Meehl *et al.*, 2007a for details). Currently, CMIP3 dataset includes 23 models, but we used those that provide all the fields requested for our analysis. Three CMIP3 dataset experiments were examined. In the 20th century climate experiment (20C) the model runs were initialized around 1860 and integrated with historical (observed) GHG, aerosol, volcanic and solar forcing. The present climate is calculated considering the 30-year period 1961–1990 (this period is recommended by the IPCC as the standard climatological baseline). In the 21st century experiments (A2 and B2) the models were integrated from initial conditions from the end of the 20C runs and subsequently forced with prescribed GHGs from scenario A2 and B2 of the IPCC SRES; (Nakicenovic and Swart, 2000), respectively. The future climate is calculated considering the 30-year period 2071–2100. It is worth noting that SRES-A2 is the IPCC scenario with the second largest atmospheric CO_2 concentrations by the end of the 21st century (about 820 ppb). In contrast, CO_2 concentrations by the end of the century in B2 (about 600 ppb) fall in the middle of the SRES range. Hereafter, Δ denotes the difference in monthly or seasonal means between 2071–2100 and 1961–1990.

A cursory inspection of the GCM data shows that all models in our subset capture the *large-scale* features of the coastal wind field, including the southerly flow at subtropical latitudes and the mean westerlies farther south, as well as the seasonal mean migration of the boundary between these two regimes. In spring and summer (Figure 4(a)) the models also exhibit a region of maximum wind speed dominated by the meridional

component off central Chile, but generally weaker than the coastal jet revealed by the QuikScat data.

The future (A2) minus present (20C) surface winds are shown in Figure 4(b). In all the models, $\Delta(U_s, V_s)$ exhibits an anti-cyclonic anomaly over the SE Pacific, just to the south of the current climate anticyclone, that leads to an increase in surface wind speed along a nearly zonal band at subtropical latitudes. The models also show a distinctive local maximum of wind speed change off the coast of central Chile ($\Delta W_s \sim 1 \text{ ms}^{-1}$), largely produced by the increase of southerly (alongshore) flow. In fall–winter, the overall pattern of the wind difference is similar, but both the oceanic band and coastal area of maximum ΔW_s are shifted a few degrees northward. The spatial patterns of ΔW_s and ΔV_s are very similar when considering B2, but with amplitude about 25% less than their counterparts in A2, which is intriguing considering the significant differences in CO_2 concentrations of these two scenarios (not shown). Recalling that the GCMs have horizontal resolution varying between 1.5° and 4° in longitude (160–430 km in the cross-shore direction) and each model has its own coastline (in some cases up to 250 km westward from the true coastline), we refrain from making further quantitative inferences concerning the wind changes.

To interpret the increase of the coastal wind in future climate, let us examine the large-scale changes in SLP over the Southern Hemisphere (SH). Figure 4(b) also shows the difference in multi-model seasonal mean SLP between A2 and 20C. A particularly strong and consistent signal among the models is an increase in SLP along the pole-ward flank of the subtropical anticyclones and

Table I. CMIP3 coupled GCM models used in this study. In those models with more than one integration per experiment, only the first run was used. Naming conventions are from the CMIP3 database.

Integration name	Institution	Horizontal grid spacing, number of vertical levels
CSIRO-Mk3.5	CSIRO Atmospheric Research, Australia	T63 (~1.875° lat-lon), L18
GFDL-CM2.0	NOAA Geophysical Fluid Dynamics Laboratory, USA	2.0° lat × 2.5° lon, L24
IPSL-CM4	IPSL/LMD/LSCE, France	3.75° lat × 2.5° lon, L19
MPI-ECHAM5	Max Planck Institute for Meteorology, Germany	T42 (~2.8° lat-lon), L20
UKMO-HadCM3	Hadley Centre for Climate Prediction, Met Office, UK	3.75° lat × 2.5° lon, L19
MIROC3.2 (medres)	CCSR/NIES/FRCGC, Japan	T42 (~2.8° lat-lon), L20
BCCR-BCM2.0	Beijing Climate Center, China	T63 (1.875lon × 1.875lat), L16
CCCMA-CGCM3	Canadian Centre for Climate Modeling and Analysis, Canada	T47 (~3.8° lat-lon), L31
GFDL-CM2.1	NOAA Geophysical Fluid Dynamics Laboratory, USA	2.0° lat × 2.5° lon, L24
GISS-MODEL ER	NASA / Goddard Institute for Space Studies, USA	4.0° lat × 5.0° lon
MIUB-ECHO-G	Meteorological Institute of the University of Bonn, Germany	2.0° lat × 2.5° lon, L24
MRI-CGCM2.3.2	Meteorological Research Institute, JAPAN	T42 (~2.8° lat-lon), L20
UKMO-HadGEM1	Hadley Centre for Climate Prediction, Met Office, UK	3.75° lat × 2.5° lon, L19
CNRM-CM3	Météo-France / Centre National de Recherches Météorologiques	T42 (~2.8° lat-lon), L45
INMCM3	Institute for Numerical Mathematics, Russia	4.0° lat × 5.0° lon, L21

a decrease at higher latitudes (e.g. Meehl *et al.*, 2007b). Such Δ SLP pattern is evident in all seasons (with minor differences in the position of the largest Δ SLP), and it has been linked with both an expansion of the Hadley circulation (Lu *et al.*, 2007) and a pole-ward shift of the SH storm track (Yin, 2005; Bengtsson *et al.*, 2006). Of particular relevance to our study are the changes over the south Pacific eastern boundary (e.g. Δ SLP along 80°W). In all the models, the difference is greatest (~2.5 hPa) at about 45°S and vanishes to the north of 25°S, leading to an increase in the meridional pressure gradient (SLP_y) along much of the subtropical west coast of South America. The increase takes place where SLP_y is weak in current climate, and therefore, it would lead to stronger southerlies because of the ageostrophic balance that prevails along the coast. For instance, during spring/summer, the observed relationship between the meridional pressure gradient and surface wind speed established at inter-annual timescales (Figure 3), the projected change in SLP_y suggests $\Delta W_s \sim 1 \text{ ms}^{-1}$ off

central Chile, well in agreement with the changes inferred from direct examination of the GCM winds.

4. Coastal winds in the PRECIS regional climate model

4.1. Model setup

The PRECIS-RCM was developed by the Hadley Centre on the basis of the atmospheric component of Hadley Centre Coupled Model, version 3 (HadCM3) (Gordon *et al.*, 2000) to generate high-resolution climate change scenarios as described in detail in Jones *et al.* (2004). It solves a hydrostatic version of the full primitive equations on a spherical-polar grid in the horizontal and a hybrid vertical coordinate with 19 levels. The PRECIS-RCM uses physical parameterization to account for the effect of clouds and precipitation, radiation and gravity wave drag upon large-scale, free-atmosphere dynamics (Jones *et al.*, 2004). Additionally, up to the bottom five model

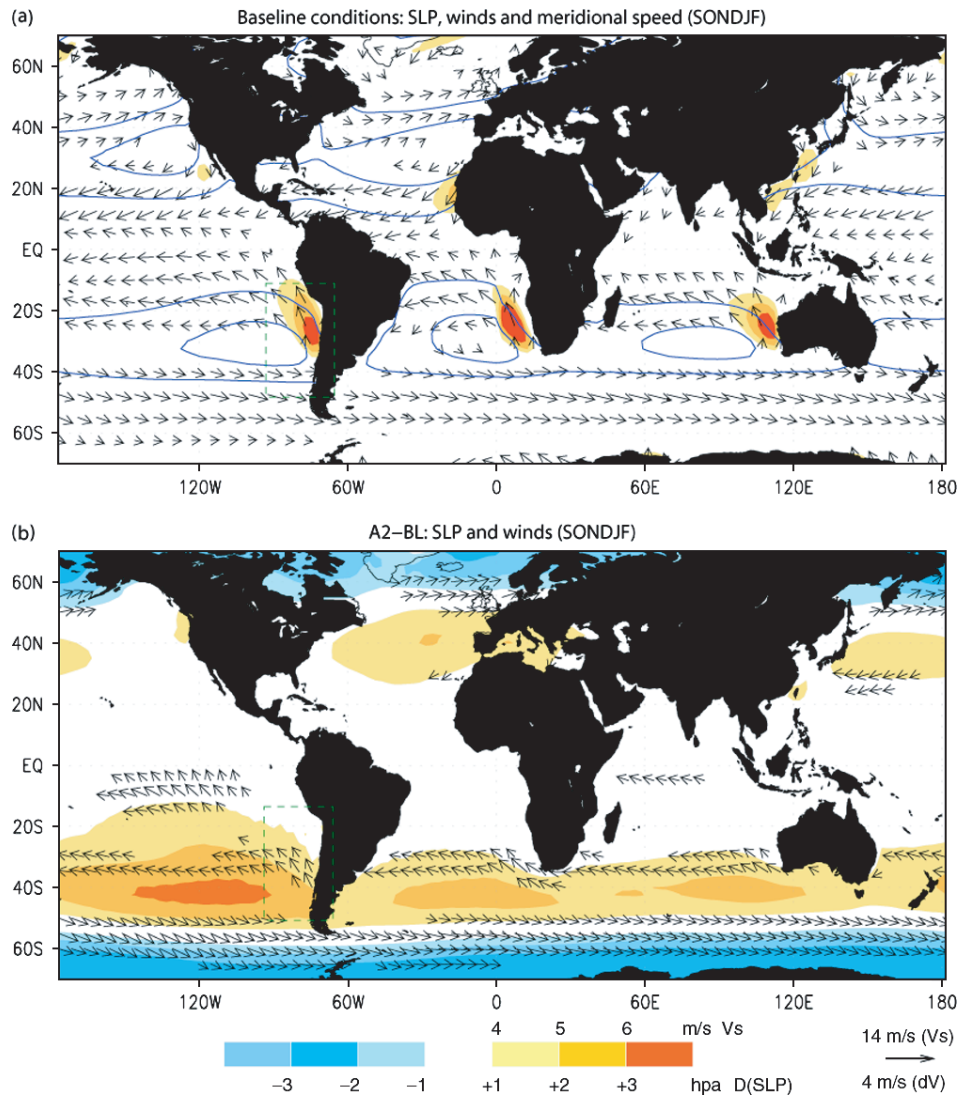


Figure 4. (a) Multi-model average of spring/summer (September to February) mean surface winds (arrows), meridional wind speed (shaded) and SLP (contours: 1012.5 and 1017.5 hPa) for the 20C experiment (1961–1990). (b) Multi-model average of spring/summer surface winds (arrows) and SLP (shaded) difference between experiments A2 (2071–2100) and 20C (1961–1990). Colour scale and vector scale are at the bottom of the figure for both panels (a) and (b). The multi-model average was obtained by interpolating the outputs from 15 coupled GCMs runs performed for CMIP3 (see Table I for details) to a uniform $2.5^\circ \times 2.5^\circ$ lat–lon grid, and subsequently averaging the long-term mean of each model.

layers can be occupied by the boundary layer, where a first-order turbulent mixing scheme is used (Smith, 1990). The energy, momentum and water exchanges between the surface and the atmosphere are calculated using the Met Office Surface Exchange Scheme (MOSES, Cox *et al.*, 1999).

Three simulations were performed, on a domain with 25 km grid spacing that extends from 18°S to 57°S and from 85°W to 62°W (Figures 1, 2 and 8 show only part of the domain). Simulation R20C spans from 1961 to 1990 and intends to represent present-day conditions. Lateral boundary conditions were obtained from the 20C integration of the HadAM3. HadAM3 is an atmospheric GCM with a relatively high horizontal resolution ($1.25^\circ \times 1.87^\circ$ lat–lon grid spacing) and improved physical parameterization (Pope *et al.*, 2001). Comparison between HadAM3 and observations reveals that the model properly simulates the large-scale atmospheric

features that shape the climate of the west coast of South America (Fuenzalida *et al.*, 2007). Surface boundary conditions (SST and sea ice extent) were derived from HadISST1, a global dataset created by the Hadley Centre by blending *in-situ* sea surface observations and satellite estimates (Rayner *et al.*, 2003). Simulations RA2 and RB2 span from 2071–2100 and were laterally forced by results from the A2 and B2 integrations of HadAM3, respectively. Future (2071–2100) SST and sea ice extent were obtained from the observed (1961–1990) HadISST1 values (that is, the inter-annual variability of the two periods is the same) plus a change and linear trend (during 2071–2100) derived from the corresponding HadCM3 runs (Jones *et al.*, 2004).

4.2. Present-day conditions

Although there is no temporal overlap between the PRECIS R20C simulation (1961–1990) and the QuikScat

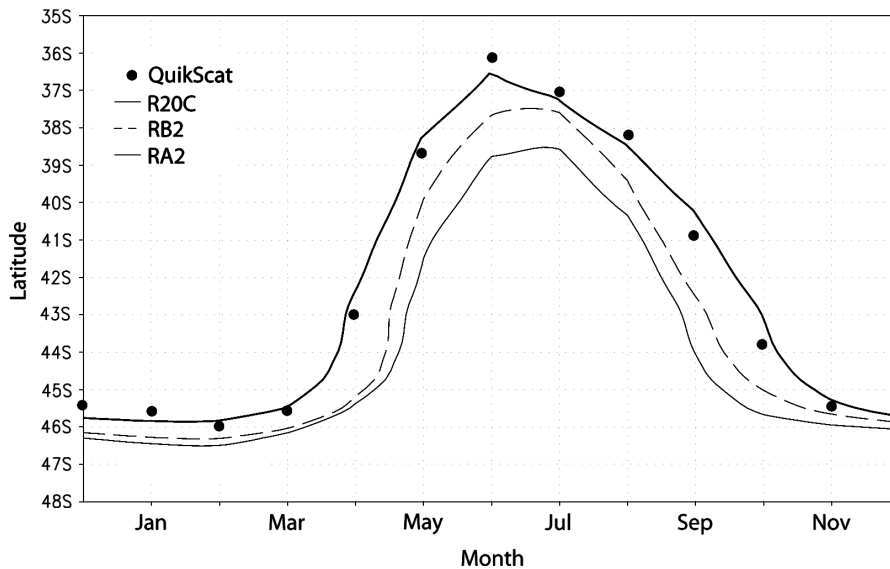


Figure 5. Mean annual cycle of the pole-ward extent of the upwelling-favourable region along the west coast of South America. For each month the limit (φ_0) was defined as the latitude at which $V_s = 0$ within the coastal strip (average of the six grid points closest to the coastline) for each dataset: QuikScat (filled circles), PRECIS R20C (thick line), PRECIS RB2 (dashed line) and PRECIS RA2 (thin line).

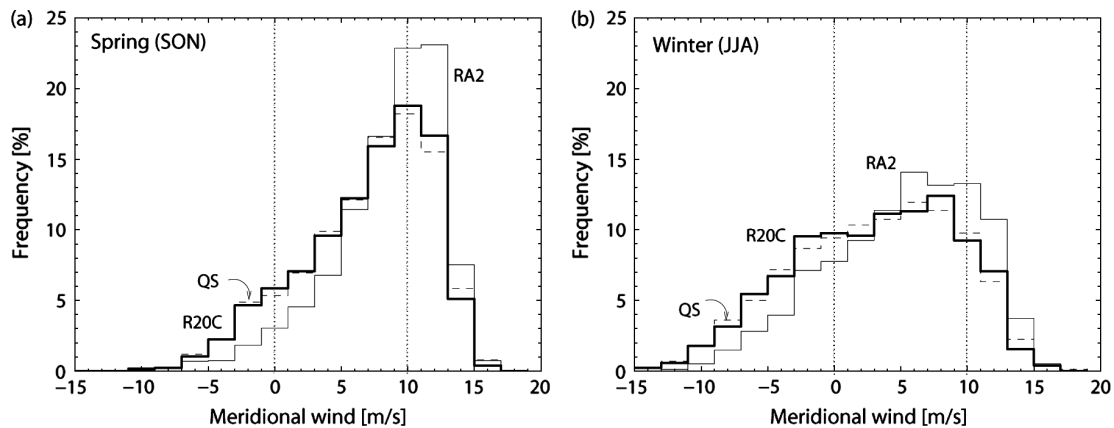


Figure 6. Histograms of daily mean values of the surface meridional wind at $33^\circ\text{S } 74^\circ\text{W}$ for (a) spring (September, October, November) and (b) winter (June, July, August). For reference, we placed vertical, dotted lines at $V_s = 0 \text{ ms}^{-1}$ (southerly/northerly flow) and $V_s = 10 \text{ ms}^{-1}$ (above that value, the wind field off central Chile often exhibits a strong coastal jet – see text). The frequency distributions were obtained for the QuikScat data (dashed line, period: 2000–2005), PRECIS R20C simulation (thick line, period: 1961–1990) and PRECIS RA2 simulation (thin line, period: 2071–2100).

observations (2000–2005), the absence of a significant trend in the coastal wind during the late 20th century allows us to compare both datasets. To this effect, Figures 1(a), (b) and 2(a), (b) show the observed and simulated spring/summer (fall/winter) mean surface winds. Overall, the simulated and observed V_s and W_s fields compare very well, with the anomaly correlations of monthly fields always above 0.7. During the ‘jet season’, coastal southerlies extend down to 42°S , both in the observations and the R20C simulation. The simulated seasonal mean wind field exhibits a coastal jet structure (delimited by the 6.5 ms^{-1} isotach) with an intensity, position and spatial extent very similar to the observations. During fall and winter, simulated coastal southerlies weaken, do not form a coastal jet and are restricted to the north of 36°S , in agreement with the observations. To further compare the long-term monthly means, we determine the southern extent of the

southerlies (φ_0) within the coastal strip. The observed and simulated φ_0 track within 1° throughout the year, (Figure 5).

The R20C daily coastal wind fields exhibit structures and variability that also compare well with the observations. The seasonal standard deviation of simulated daily V_s is relatively modest (2 ms^{-1}) off northern Chile and increases (6 ms^{-1}) farther south, similar to the pattern derived from QuikScat observations (not shown). In GM05, coastal jet days were objectively identified using a cluster analysis applied upon the wind speed field. It turned out that nearly all days in which $V_s \geq 10 \text{ ms}^{-1}$ along the subtropical coast were associated with strong jet events. In this work, we did not perform a cluster analysis, but Figure 6 shows the histograms of daily V_s at $33^\circ\text{S}–74^\circ\text{W}$ for both QuikScat and R20C during spring and winter. In both seasons, the frequency distributions are very similar, and both suggest that strong jets are

present about 20% (10%) of days during the spring (winter).

4.3. Future conditions

The spring/summer mean surface winds for the RA2 simulation are shown in Figure 1(c), and their differences with R20C are shown in Figure 1(d); the fall/winter fields are shown in Figure 2(c–d). Consistent with the GCMs results, future PRECIS fields show a spin-up of the anticyclonic circulation over the SE Pacific in the future and an increase in surface wind speed ($\Delta W_s \sim 1 \text{ ms}^{-1}$) at subtropical latitudes in all seasons. In the coastal zone, the projected increase in wind speed is largely produced by stronger southerlies off central (southern) Chile during fall/winter (spring/summer). The spatial pattern of ΔW_s for RB2 is very similar to RA2, but with an amplitude about 25% smaller (not shown).

The future climate not only exhibits stronger southerlies along the subtropical coast, but the upwelling-favourable region extends farther south, or, alternatively, there is an extended upwelling-favourable season at southern latitudes. The spatial perspective is presented in Figure 5, where the monthly mean φ_0 is plotted for each simulation. The pole-ward limit of the coastal

southerlies reaches its southernmost position (46°S) in December/January in all cases. In current conditions, the equator-ward displacement of φ_0 begins in March, reaching 36°S in June. In simulation RA2, the equator-ward displacement of φ_0 is delayed until April and is more gradual, with φ_0 only reaching 38°S in June. The spring migration of φ_0 to southern Chile in RA2 also occurs earlier than in R20C, so that $\Delta\varphi_0 \sim 4^\circ \sim 450 \text{ km}$ around April and September. The temporal perspective is portrayed in Figure 7(a) by the time series of V_s at a coastal point in southern Chile ($39^\circ\text{S}-75^\circ\text{W}$). The upwelling season ($V_s > 0$) is about 2 months longer in RA2 compared with R20C due to an earlier onset and later demise. In Figure 7(a) a strengthening of the southerlies is also evident, with the largest $\Delta V_s \sim 1.5 \text{ ms}^{-1}$ at the height of the summer. We used a one-tailed Student t -test to gauge ΔV_s , which results statistically different from 0 at the 95% level from September to February at this southern location.

Let us turn our attention to north-central Chile. Figure 7(b) shows the time series of V_s at $33^\circ\text{S}-73^\circ\text{W}$. Here, $\Delta V_s > 0$ is statistically significant from April to November and is greatest in mid-winter (2 ms^{-1}). Considering $V_s \geq 6 \text{ ms}^{-1}$ as indicative of jet conditions,

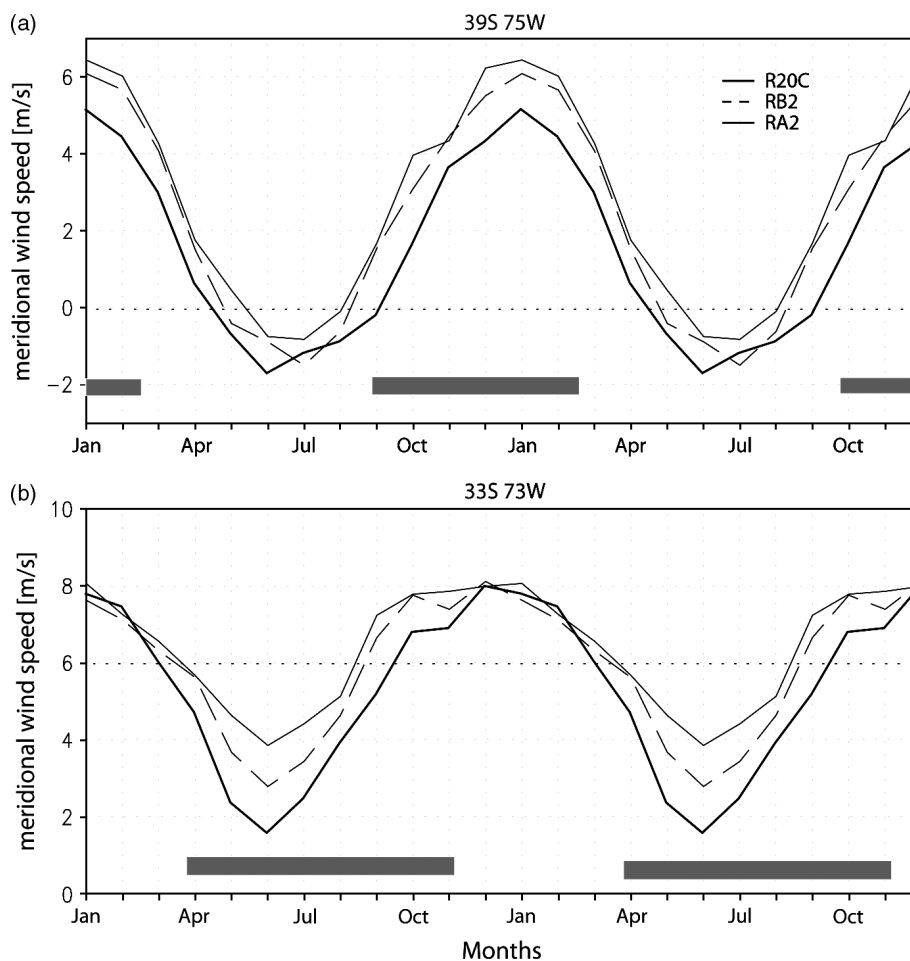


Figure 7. Mean annual cycle of the surface meridional wind at (a) $39^\circ\text{S}-75^\circ\text{W}$ and (b) $33^\circ\text{S}-73^\circ\text{W}$. Results for the three PRECIS simulations are shown: R20C (thick line, 1961–1990), RB2 (dashed line, 2071–2100) and RA2 (thin line, 2071–2100). Grey bars at the bottom indicate months in which $\Delta V_s > 0$ is statistically significant at the 95% confidence level according to a one-tailed Student's t -test.

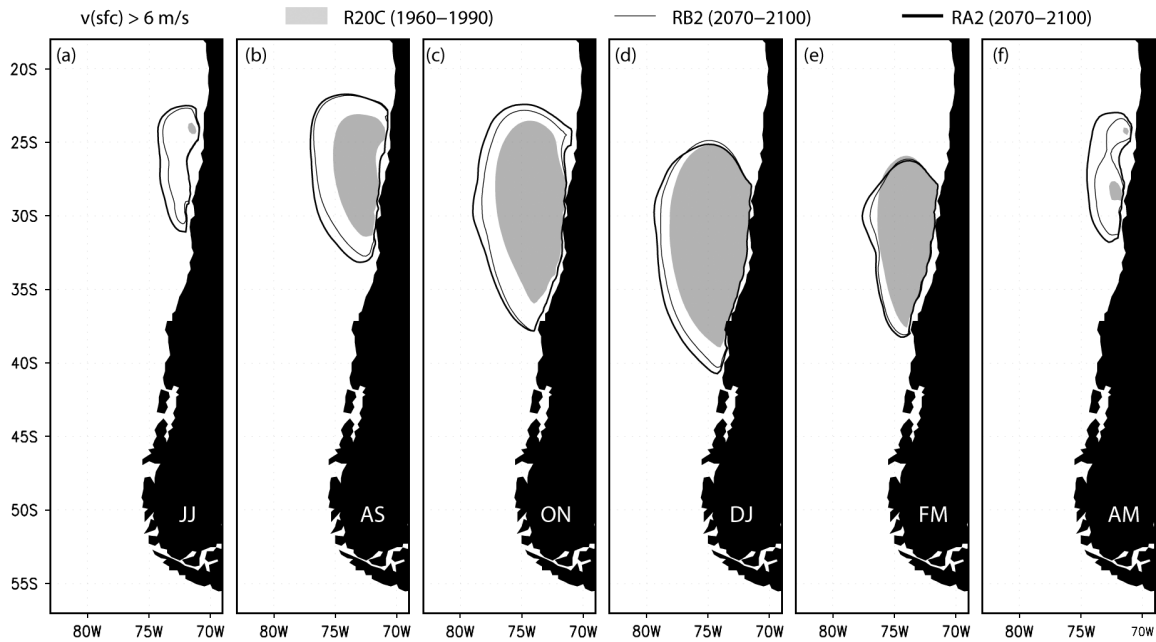


Figure 8. Bi-monthly maps of the ‘mean’ jet, defined as the region with $V_s > 6 \text{ ms}^{-1}$ (see text), for the three PRECIS simulations: R20C (shaded area), RB2 (area enclosed by the thin line) and RA2 (area enclosed by the thick line). From left to right, the months are (a) June, July, (b) August, September, (c) October, November, (d) December, January, (e) February, March, and (f) April, May.

the jet season at subtropical latitudes also will extend for about two extra months in RA2. To visualize the ‘mean’ jet, the area enclosed by $V_s = 6 \text{ ms}^{-1}$ is shown in Figure 8. In the future (both RA2 and RB2), the mean jet prevails through the year, albeit smaller in winter, in contrast with the present-day conditions when the jet is absent in fall/winter. Note that in December, January, February and March the mean jet roughly covers the same area and has the same intensity in R20C, RA2 and RB2 (Figures 7(b) and 8(d–e)). The level-off of ΔV_s at the height of the ‘jet season’ could be partially associated with the dynamical nature of the coastal jet in which the meridional pressure gradient is balanced by the frictional force, roughly proportional to V_s .

The increment in V_s off the subtropical coast during winter/spring is related with changes in distribution and variability of daily values, partially illustrated by the histograms of V_s at 33°S – 74°W (Figure 6). During spring, the RA2 distribution is shifted to the right of the R20C distribution, so the frequency of strong jet days ($V_s > 10 \text{ ms}^{-1}$) increases up to 33% (20% in R20C) at the expense of a reduction of northerly flow days. Future jet events become longer (typically 7–15 days) but no more intense than current events. In winter, the RA2 distribution exhibits a significant reduction of the days in which $V_s < 0$ with respect to R20C, but no major increase in the frequency of jet events, consistent with a marked reduction in the day-to-day standard deviation of V_s noted in this season.

5. Discussion

The geographic pattern of projected surface air temperature change (Figure 9) shows an area of minimum

warming over the southern ocean that extends equatorward along the west coast of South America – as far north as 20°S – and even intensifies westward over the SE Pacific. Considering the 2071–2100 period under the A2 scenario, the CMIP3 multi-model mean surface warming is $3.5 \pm 0.45^\circ\text{C}$ for the whole globe, but only $1 \pm 0.1^\circ\text{C}$ for the southern ocean and parts of the SE Pacific (Figure 9, see also Meehl *et al.*, 2007b). The warming off central Chile is three times lower than its counterpart over the adjacent South American continent, reflecting in part the relatively high thermal inertia of the ocean but still two times lower than the mean warming over oceanic areas at the same latitude, suggesting the action of a regional-scale mechanism. We hypothesize here that such a mechanism could involve a wind-driven SST *cooling* along the Chilean coast and the subsequent offshore spread of the cold waters throughout near-surface horizontal advection. Alternative mechanisms, including cloud-induced changes in the radiation balance in this stratocumulus-capped region will be investigated elsewhere. Further, the projected changes in surface winds, upwelling and SST are likely to trigger changes in the marine environment that would eventually affect the regional fishery industry.

The projected strengthening of the southerly winds along the coast can modify the energy balance of the oceanic mixed layer in several ways. First, stronger winds will increase the latent heat flux (LHF), a major term of the balance off central Chile (e.g. Yu and Weller, 2007). At 33°S – 73°W , for instance, LHF changes from -70 Wm^{-2} in R20C to -100 Wm^{-2} in RA2. The PRECIS results also suggest a future increase in net shortwave radiation (from 207 to 220 Wm^{-2}), consistent with less cloudy conditions during jet events (GM05),

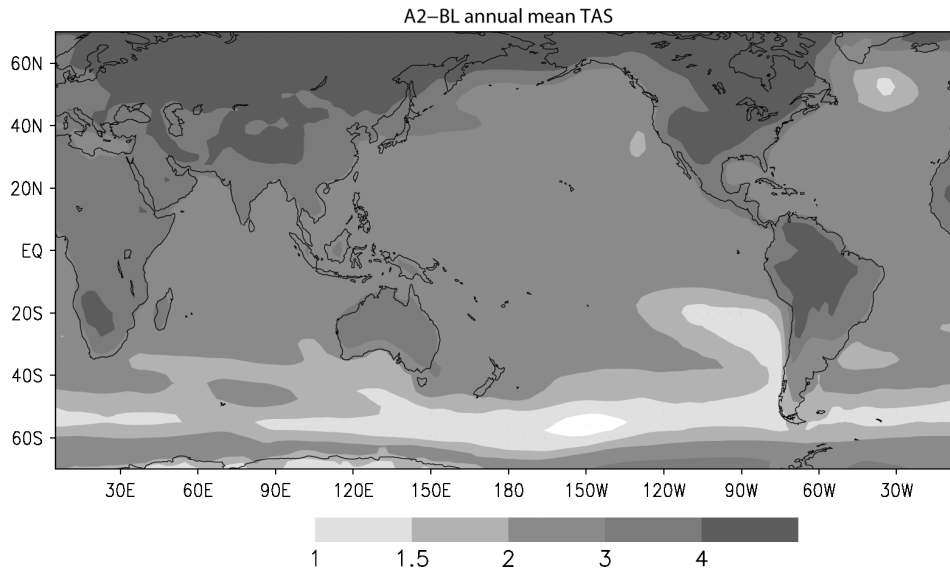


Figure 9. (a) Multi-model average of annual mean surface air temperature difference between A2 (2071–2100) and 20C (1961–1990) simulations, shaded according to the scale at the bottom. The multi-model average was obtained by interpolating the outputs from 15 coupled GCMs runs performed for CMIP3 (see Table I for details) to a uniform $2.5^\circ \times 2.5^\circ$ lat–lon grid, and subsequently averaging the long-term mean of each model.

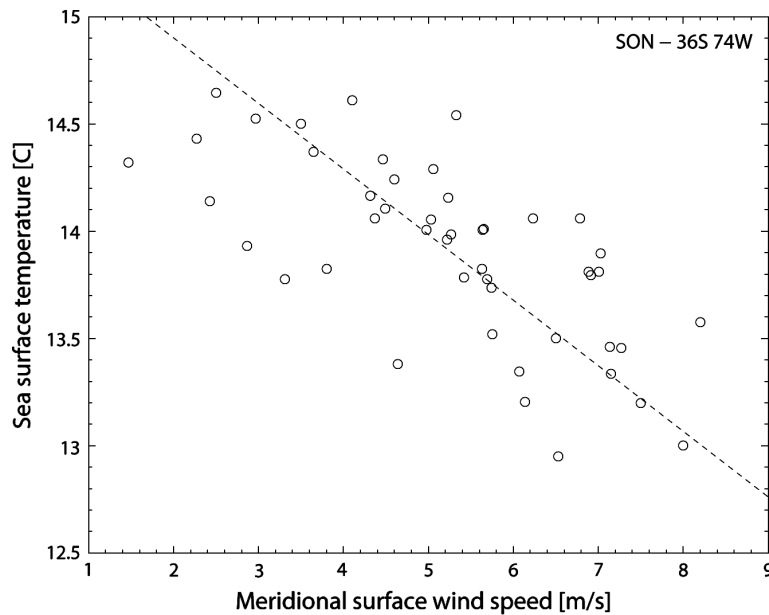


Figure 10. Scatter plot between spring (September, October, November) mean values of NCEP-NCAR reanalysis surface meridional wind (horizontal axis) and sea surface temperature at 36°S – 74°W , considering the period 1958–2002. SST time series was obtained from the extended-reconstructed SST dataset (Smith and Reynolds, 2004).

that combined with ΔLHF and minor changes in sensible heat flux and longwave radiation, leads to a 50% reduction of the net energy in the ocean. Recall that PRECIS fluxes were calculated using prescribed SST, so these numbers are preliminary.

The effect of the stronger coastal southerlies upon advection and diffusion within the mixed layer are more difficult to evaluate, because we do not have high-resolution predictions of the changes in the ocean thermal structure. Coupled ocean–atmosphere RCM simulations are necessary to obtain such predictions. Nevertheless, the increase in Ekman transport and Ekman pumping, in response to the stronger southerlies, will

likely lead to an additional surface cooling given the marked stratification and shallow mixed layer of the subtropical SE Pacific. The coupled GCMs do capture all the aforementioned atmospheric and oceanic effects, but given their coarse resolution, they may underestimate the magnitude of the relative SST cooling.

An alternative, preliminary estimate of the wind-driven changes can be obtained using historical information. Figure 10 shows the scatter plot between September–October–November averages of meridional wind and SST off central Chile for the period 1958–2002. It indicates that inter-annual variations in local wind explain roughly 50% of the variance in SST (we do not have

a reason to expect a SST control on local winds at this timescale). Similarly significant, albeit weaker, correlations are found in other seasons. The scatter in Figure 10 is likely caused by the non-local processes that modulate SST, such as intra-seasonal wave activity trapped against the coast (Hormazabal *et al.*, 2001). The observed linear relationship ($\partial\text{SST}/\partial V_s \sim -0.5^\circ\text{C}/\text{ms}^{-1}$) and the predicted increase in coastal winds ($\Delta V_s \sim 1.5 \text{ ms}^{-1}$) imply $\Delta\text{SST} \sim -0.7^\circ\text{C}$. This value roughly coincides with cooling anomaly of the SE Pacific with respect to the rest of the subtropical oceans.

6. Conclusions

On the basis of 15 coupled GCM and high-resolution RCM simulations, we have examined the changes in surface wind off the western coast of subtropical South America (north-central and southern Chile) projected for the end of the 21st century under the A2 and B2 IPCC scenarios. Our main findings are as follows:

- Near-coastal wind speed in the A2 scenario will increase $\sim 1 \text{ ms}^{-1}$ ($\sim 15\%$) with respect to the present-day conditions. This signal is very consistent among the GCMs, occurs throughout the year, and is largely produced by a strengthening of the coastal southerlies. The seasonal patterns of coastal wind change are very similar when considering B2, but with amplitudes about 25% less than their A2 counterparts.
- Consistent among the GCMs is a marked increase in SLP (2–3 hPa) at mid-latitudes across much of the oceans in the SH. In contrast, SLP does not change significantly at subtropical latitudes, thus producing an enhanced meridional pressure gradient conducive to a strengthening of the low-level coastal jet.
- The PRECIS-RCM high-resolution simulation of the 20th century was capable of capturing the seasonal and synoptic variability of the coastal winds off western subtropical South America, including an accurate representation of the seasonality, frequency and structure of the coastal jet events.
- The PRECIS results confirm the strengthening of the coastal wind speed and allow a more detailed evaluation of the changes. During spring and summer, the largest increments in meridional wind occur between 37°S and 41°S , just to the south of the seasonal coastal jet. During fall and winter, the strengthening of the southerlies occurs at subtropical latitudes, maintaining a seasonal jet year-round. Off southern Chile, (around 40°S) the upwelling-favourable season is about two months longer in the future. Future coastal jet events during spring are more frequent and last longer than present-day events.
- Stronger winds lead to SST cooling along the Chilean coast because of enhanced surface fluxes and probably because of more active upwelling. Cold waters can spread offshore through near-surface horizontal advection and enhanced oceanic eddy activity. CMIP3-coupled GCMs already indicate of such relative

regional cooling in a global-warming context, but coupled RCM simulations are needed to capture the true impact of enhanced southerlies in SST.

Acknowledgements

The PRECIS simulations were performed for the ‘Study on Climate Variability for Chile during the 21st century’ supported by the National Environmental Committee (CONAMA-Chile). We acknowledge the modelling groups for making their simulations available for analysis, the Program for Climate Model Diagnosis and Intercomparison (PCMDI) for collecting and archiving the CMIP3 model output, and the WCRP’s Working Group on Coupled Modelling (WGCM) for organizing the model data analysis activity. The WCRP CMIP3 multi-model dataset is supported by the Office of Science, U.S. Department of Energy. Both authors are supported by CONICYT (Chile) Grant ACT-19. The manuscript was improved through the comments of two anonymous reviewers.

References

- Bengtsson L, Hodges KI, Roeckner E. 2006. Storm tracks and climate change. *Journal of Climate* **19**: 3518–3543.
- Chaigneau A, Pizarro O. 2005. Mean surface circulation and mesoscale turbulent flow characteristics in the eastern South Pacific from satellite tracked drifters. *Journal of Geophysical Research* **110**: C05014, DOI:10.1029/2004JC002628.
- Christensen JH, Hewitson B, Busuioc A, Chen A, Gao X, Held I, Jones R, Kolli RK, Kwon RT, Laprise R, Magaña V, Mearns CG, Menendez CG, Raisanen J, Rinke A, Sarr A, Whetton P. 2007. Regional climate projections. *Climate Change 2007: The Physical Science Basis. Contribution of Working Group I to the Fourth Assessment Report of the Intergovernmental Panel on Climate Change*. Cambridge University Press: New York.
- Cox PM, Betts RA, Bunton CB, Essery R, Rowntree R, Smith J. 1999. The impact of the new land surface physics on the GCM simulation of climate and climate sensitivity. *Climate Dynamics* **15**: 183–2003.
- Fuenzalida H, Aceituno P, Falvey M, Garreaud R, Rojas M, Sanchez R. 2007. Study on climate variability for Chile during the 21st century. In *Technical Report prepared for the National Environmental Committee*, Spanish, Santiago, Chile. Available on-line at <http://www.dgf.uchile.cl/PRECIS> (August 2007).
- Garreaud R, Munoz R. 2005. The low-level jet off the subtropical west coast of South America: structure and variability. *Monthly Weather Review* **133**: 2246–2261.
- Gordon C, Cooper C, Senior CA, Banks J, Gregory JM, Johns TC, Mitchell JFB, Wood RA. 2000. The simulation of SST, sea ice extent and ocean heat transport in a version of the Hadley Centre coupled model without flux adjustments. *Climate Dynamics* **16**: 147–168.
- Hormazabal S, Shaffer G, Letelier J, Ulloa O. 2001. Local and remote forcing of sea surface temperature in the coastal upwelling system off Chile. *Journal of Geophysical Research* **106**(C8): 16,657–16,672.
- Jones RG, Noguer M, Hassell DC, Hudson D, Wilson SS, Jenkins GJ, Mitchell JFB. 2004. Generating high resolution climate change scenarios using PRECIS, Met. Office Hadley Center, Exeter, UK, 40.
- Kalnay E, Kanamitsu M, Kistler R, Collins W, Deaven D, Gandin L, Iredell M, Saha D, White G, Woollen J, Zhu Y, Chelliah M, Ebisuzak W, Higgins W, Janowiak J, Mo KC, Ropelewski C, Wang J, Leetma A, Reynolds R, Dennis J. 1996. The NCEP/NCAR 40-years reanalysis project. *Bulletin of the American Meteorological Society* **77**: 437–472.
- Lu J, Vecchi GA, Reichler T. 2007. Expansion of the Hadley cell under global warming. *Geophysical Research Letters* **34**: L06805, DOI:10.1029/2006GL028443.
- Meehl GA, Covey C, Delworth T, Latif M, McAvaney B, Mitchell JB, Stouffer R, Taylor K. 2007a. THE WCRP CMIP3 multimodel

- dataset: a new era in climate change research. *Bulletin of the American Meteorological Society* **88**: 1383–1394.
- Meehl GA, Stocker TF, Collins WD, Gaye AT, Gregory JM, Kitoh A, Knutti R, Murphy JM, Noda A, Raper S, Watterson IG, Weaver AJ, Zhao ZC. 2007b. Global climate projections. *Climate Change 2007: The Physical Science Basis. Contribution of Working Group I to the Fourth Assessment Report of the Intergovernmental Panel on Climate Change*. Cambridge University Press: New York.
- Munoz R, Garreaud R. 2005. Dynamics of the low-level jet off the subtropical west coast of South America. *Monthly Weather Review* **133**: 3661–3677.
- Nakicenovic N, Swart R (eds). 2000. *Special Report on Emissions Scenarios*. Cambridge University Press: New York.
- Pope VD, Pamment JA, Jackson DR, Slingo A. 2001. The representation of water vapor and its dependence on vertical resolution in the hadley centre climate model. *Journal of Climate* **14**: 3065–3085.
- Rayner NA, Parker DE, Horton EB, Folland CK, Alexander LV, Rowell DP, Kent EC, Kaplan A. 2003. Global analyses of sea surface temperature, sea ice, and night marine air temperature since the late nineteenth century. *Journal of Geophysical Research* **108**(D14): 4407, DOI:10.1029/2002JD002670.
- Rutllant J, Montecino V. 2002. Multiscale upwelling forcing cycles and biological response off North-central Chile. *Revista Chilena de Historia Natural* **75**: 217–231.
- Shaffer G, Hormazábal S, Pizarro O, Salinas S. 1999. Seasonal and interannual variability of currents and temperature over the slope off central Chile. *Journal of Geophysical Research* **104**: 29951–29961.
- Smith TM, Reynolds RW. 2004. Reconstruction of monthly mean oceanic sea level pressure based on COADS and station data (1854–1997). *Journal of Atmospheric and Oceanic Technology* **21**: 1272–1282.
- Smith RNB. 1990. A scheme for predicting layer clouds and their water content in a general circulation model. *Quarterly Journal of the Royal Meteorological Society* **116**: 435–460.
- Yin JH. 2005. A consistent poleward shift of the storm tracks in simulations of 21st century climate. *Geophysical Research Letters* **32**: L18701, DOI:10.1029/2005GL023684.
- Yu L, Weller RA. 2007. Objectively analyzed air–sea heat fluxes for the global ice-free oceans (1981–2005). *Bulletin of the American Meteorological Society* **88**: 527–539.
- Yuras G, Ulloa O, Hormazábal S. 2005. On the annual cycle of coastal and open ocean satellite chlorophyll off Chile (18°–40°S). *Geophysical Research Letters* **32**: L23604, DOI:10.1029/2005GL023946.